Int. J. Electrochem. Sci., 17 **(2022)** Article Number: 220529, doi: 10.20964/2022.05.23

International Journal of
ELECTROCHEMICAL
SCIENCE
www.electrochemsci.org

Short Communication

Effective Combination of Fe_2O_3 with 3D Graphene Foam for Preparation of Binder-Free Anode for Sodium-Ion Batteries

Xin Wang[1], *Hengxu Liu*[1], *Lianyang Wang*[2], *Dongping Li*[1,*]

[1] School of Materials Science and Chemical Engineering, Harbin University of Science and Technology, Harbin 150080, PR China.
[2] School of Materials Science and Engineering, Jiamusi University, Jiamusi 154007, PR China
[*]E-mail: lidongping@hrbust.edu.cn

Received: 8 January 2022 / *Accepted:* 17 February 2022 / *Published:* 5 April 2022

This research created a self-supporting material composed of Fe_2O_3 nanorods and 3D graphene foam (3DGF). The graphene foam which was intimately combined with the Fe_2O_3 nanorods effectively alleviated the volume expansion and increased the cycle stability. The graphene foam framework offered a continuous electron transfer pathway that enhanced the conductivity of the electrode material. Fe_2O_3@3DGF annealed at 400°C exhibited superior sodium storage properties with a high reversible capacity of 398 $mAh \cdot g^{-1}$ after 200 cycles at a current density of 500 $mA \cdot g^{-1}$.

Keywords: Fe_2O_3; 3D graphene foam; Combination; Anode material; Sodium-ion batteries.

1. INTRODUCTION

In recent years, the demand for high-energy rechargeable lithium-ion batteries has increased in various industries such as automobiles, electron devices and so on [1-4]. Lithium-ion batteries have been successfully commercialized, however, the high costs and limited resources are still challenges. These prompt researchers to make significant efforts on the development of sodium-ion batteries (SIBs) as potential alternatives to lithium-ion batteries [5-9]. Indeed, owing to the natural abundance, low cost and environmental friendliness of sodium, large efforts have been devoted to SIBs [10-13]. Recently, various materials have been intensively studied to better host larger Na^+ ions. Metal oxides with unique structural features have become important candidate electrode materials for SIBs in energy storage and conversion [14-17]. Specifically, among Fe-based high-energy battery materials, Fe_2O_3 has been considered as the most promising candidate for SIBs. This is due to its high theoretical capacity (1007$mAh \cdot g^{-1}$), abundance and environmental friendliness [18-19]. However, Fe_2O_3 still has limitations in achieving high reversible

capacity and cycling stability for low electrical conductivity and large volume expansion. To solve the above issues, various strategies such as fabrication of Fe_2O_3 with carbon coating, nanotubes and nanofibers have been attempted [20-21]. Therefore, the use of carbon materials to modify Fe_2O_3 anodes has been recognized as an efficient way to improve the electrical conductivity and buffer the volume expansion during the charging and discharging processes. However, according to pertinent literature, the optimization of electrochemical performance in Fe_2O_3 anodes is still needed [22-24]. Meanwhile, a recent study has shown that the modification of electrode material structure is critical for improving electrochemical activity and shortening of electron transport paths in SIBs [25].

In this work, we developed a nanorod array Fe_2O_3@3DGF as the anode material for SIBs by annealing α-FeOOH@3DGF as precursor through a one-step hydrothermal method at a certain temperature. The 3DGF acted as a strong mechanical matrix, which sustained the volume changes during cycling and electronic conductive network. Owing to its superior structural advantages, the as-prepared Fe_2O_3@3DGF showed excellent conductivity, high performance and outstanding stability and was considered as a safer electrode material for SIBs.

2. EXPERIMENTAL

2.1 α-FeOOH@3DGF synthesis

The precursor nanorod α-FeOOH@3DGF was synthesized by a hydrothermal method. Briefly, 1 mmol $FeCl_3 \cdot 6H_2O$ and 15 mmol urea were dissolved in 70 mL de-ionized (D.I.) water. The solution was transferred to a 100 ml Teflon stainless steel autoclave with a piece of 3D graphene foam and was heated at 200℃ for 24 hours. After cooling to room temperature, the α-FeOOH@3DGF was obtained by washing several times with D.I. water and ethanol.

2.2 Fe_2O_3@3DGF synthesis

The α-FeOOH@3DGF was annealed at 400℃ under a flowing argon atmosphere with a temperature rise rate of 10 $^oC \cdot min^{-1}$ for 4 hours.

2.3 Electrochemical analysis

The CR2032-type battery assembled in an argon-filled glove box was used for the electrochemical experiment. The as-synthesized Fe_2O_3@3DGF was a free-standing material. Cells were assembled without any binders. Glass fiber (Whatman GF) and Na metal were used as separator and counter electrode, respectively. The electrolyte employed was 1M $NaPF_6$ in ethyl methyl carbonate. The charging and discharging measurement voltages ranged from 0.3V to 3.0V at different current densities using LAND test system. Cyclic voltammetry (CV) was performed with an electrochemical workstation CHI760 in the voltage range from 0.3V to 3.0V at a scan rate of $0.1mVs^{-1}$ to $1mVs^{-1}$.

3. RESULTS AND DISCUSSION

3.1 Microstructure of Fe_2O_3@GF

The schematic illustration for the synthesis of Fe_2O_3@3DGF was shown in Figure 1. The precursor α-FeOOH@3DGF was first prepared by a one-step hydrothermal method. The as-prepared α-FeOOH@3DGF was then annealed in argon for 4 hours to form Fe_2O_3@3DGF. The detailed procedure was described in section 2.

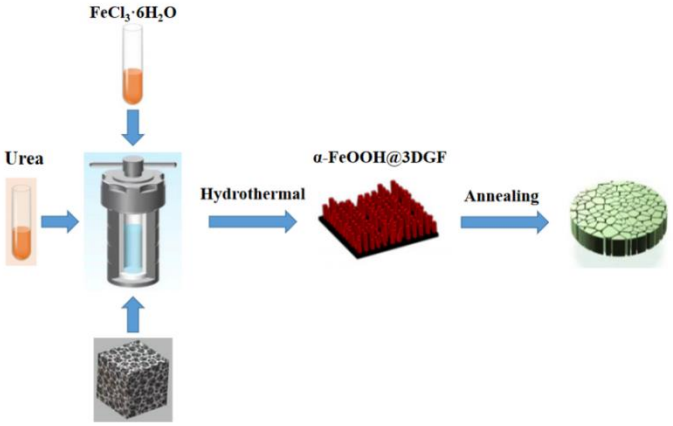

Figure 1. Schematic illustration for the synthesis process of precursor α-FeOOH@3DGF and Fe_2O_3@3DGF nanorods

The formation and phase transformation reactions of α-FeOOH and Fe_2O_3 were shown as follows [26]:

$$Fe^{2+}+2H_2O \rightarrow Fe(OH)_2+2H^+ \quad (1)$$

$$4Fe(OH)_2+O_2 \rightarrow 4FeOOH+2H_2O \quad (2)$$

$$2FeOOH \rightarrow Fe_2O_3+H_2O \quad (3)$$

The phase compositions and structure of products were confirmed by X-ray diffraction (XRD) patterns, Figure 2 illustrated the phase evolution of precursor α-FeOOH@3DGF and Fe_2O_3@3DGF. All XRD diffraction peaks were indexed to pure α-FeOOH phase (JSPDS No. 34-1266) [5] and graphene foam. No other peaks appeared, indicating the high purity of the prepared samples. When the annealing temperature was 400°C, all the peaks located at (110), (113), (116) and (300) were assigned to Fe_2O_3 (JSPDS No. 33-0664) [7], indicating the reduction of hydroxyl oxidize iron. No other peaks appeared, indicating precursor α-FeOOH@3DGF was converted completely to Fe_2O_3@3DGF.

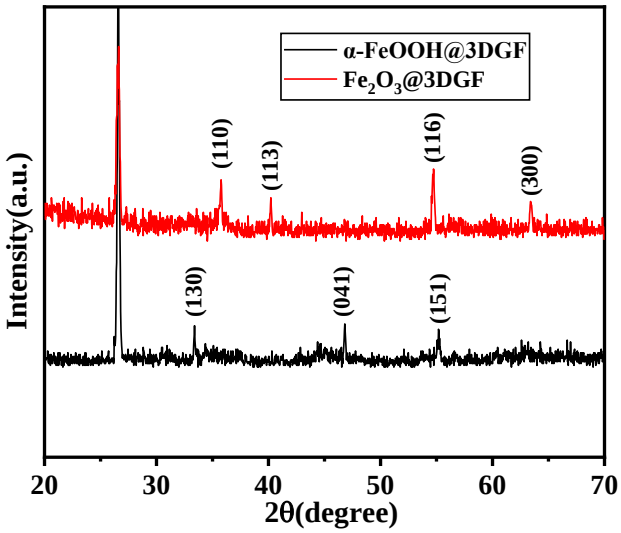

Figure 2. XRD patterns of precursor α-FeOOH@3DGF and Fe_2O_3@3DGF

Figure 3a showed a representative SEM image of Fe_2O_3@3DGF with a shuttle-like morphology. After annealing, the entire nanorod was arrayed uniformly in the graphene foam frameworks. The higher magnification images in Figure 3b confirmed that the diameter and length of the nanorods were about 100nm and 200-300nm, respectively.

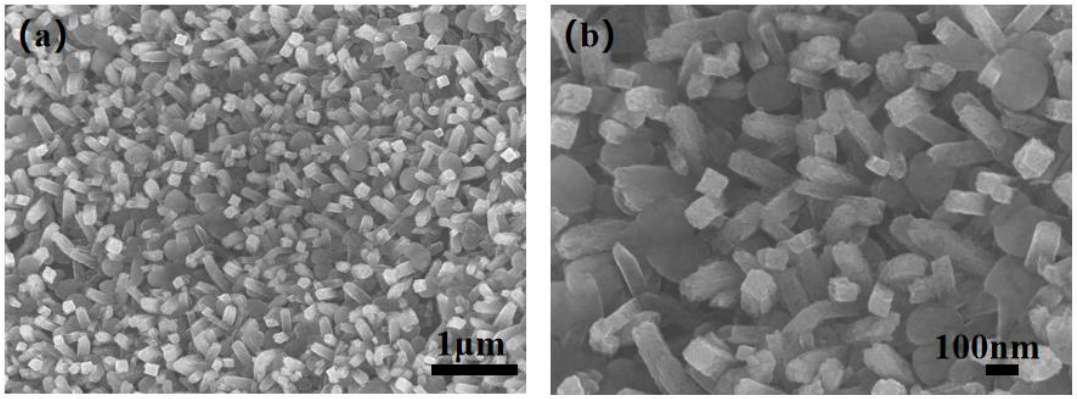

Figure 3. SEM images of Fe_2O_3@3DGF for 4h annealing in argon (a) Low-magnification; (b) High-magnification

3.2 Electrochemical characterization

In order to evaluate the sodium storage ability of Fe_2O_3@3DGF, CR2032-type cells with Na metal as the counter electrode were assembled. Experiments were performed in the voltage range from 0.3V to 3V at room temperature. CV curve of the as-prepared Fe_2O_3@3DGF for the first, second and third cycles at scan rate of $0.5mV \cdot s^{-1}$ was shown in Figure 4. During the first reduction process, two strong reduction peaks were observed at 0.62V and 1.1V, which were attributed to the initial sodium ion

insertion to the crystal structure and reduction of $Fe2^{+}/Fe^{3+}$ to Fe^{0}, respectively. During the oxidation process, the anodic peaks appear at 1.6 V, 1.3 V and 0.9 V, which corresponded to the oxidation of Fe^{0} to Fe^{2+} followed by oxidation of Fe^{2+} to Fe^{3+} [1, 27-28]. Theoretically, the number of oxidation and reduction reaction peaks should be similar. However, the results for Fe_2O_3@3DGF were different which may be due to the slow reaction process and the limitation of the test conditions. In the subsequent second and third charge-discharge cycles, we observed good overlap of CV curves which implied good reversibility and stability of the electrochemical reaction [29].

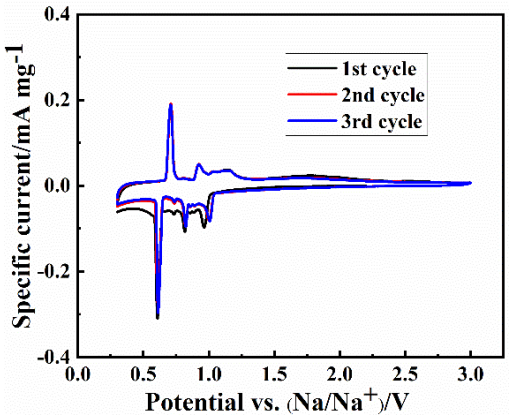

Figure 4. CV curves of Fe_2O_3@3DGF at scan rate of 0.5mV·s^{-1}

The long-term cycling behaviour and coulombic efficiency of Fe_2O_3@3DGF were then investigated at a current density of 500 mA·g^{-1}. As shown in Figure 5, the first discharge and first charge specific capacities of Fe_2O_3@3DGF were 575 mAh·g^{-1} and 542 mAh·g^{-1}, respectively with a coulomb efficiency that reached to 92.6%. With the increase in charge-discharge cycles, Fe_2O_3@3DGF exhibited excellent cycling stability until 200 cycles at 398 mAh·g^{-1} which corresponded to a retention capacity of 73.4%. The coulombic efficiency of the Fe_2O_3@3DGF electrode rapidly increased to 99% after a few cycles.

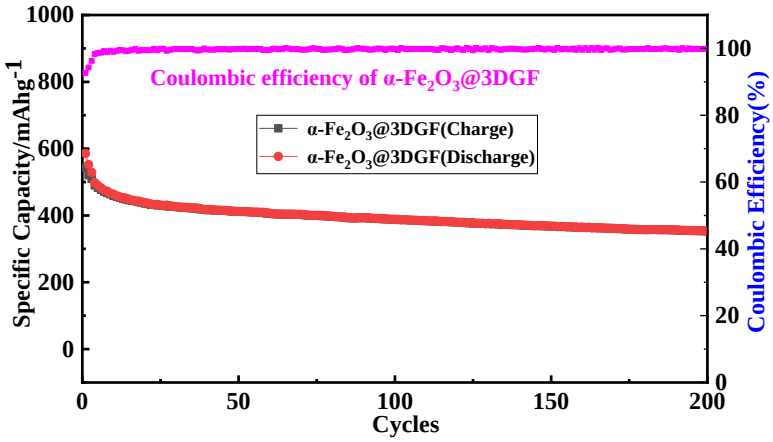

Figure 5. Cycling performance with the coulombic efficiency of Fe_2O_3@3DGF at a current of 500mA·g^{-1}

In recent years, scientists had found the presence of pseudocapacitance contribution. This had been confirmed to have fast charging and discharging characteristics [2,3]. CV tests were used at various scan rates between 0.1mVs^{-1} and 10.1mVs^{-1} to evaluate the electrode process kinetics of Fe_2O_3@3DGF. The results were shown in Figure 6a. The relationship between scan rate (v) and peak current (i) was described by equation 4:

$$i=av^b \quad (4)$$

where a and b were variable parameters. When the value of b approached to 1, the electrochemical process was controlled by pseudo-capacitance. Meanwhile, when the value of b approached to 0.5, the process was controlled by ionic diffusion behaviour [4]. The oxidation peaks at 0.9 V and 1.2V were named Peak 1 and Peak 2, respectively. The reduction peaks at 0.65 V and 1.0V were named Peak 3 and Peak 4, respectively. They showed that Fe_2O_3 was reduced to Fe during the charge process with the creation of Na_2O and the Fe was oxidized to Fe^{2+}/Fe^{3+} during the discharge process, respectively.

Moreover, equation 4 can be given in another form by equation (5):

$$\log(i)=\log(a)+b\log(v) \quad (5)$$

Figure 6b displayed the log (i) vs. log (v) plot of peaks 1, 2, 3 and 4 with b-values of 0.81 and 0.77. The kinetics of Fe_2O_3@3DGF were largely controlled by pseudocapacitive behaviour (Figure 6b). The percentage of pseudocapacitive contribution was calculated by equation 6.

$$i=k_1v+k_2v^{1/2} \quad (6)$$

where k_1 and k_2 represented capacitive and diffusion contributions, respectively. Figure 6c exhibited the percentage contribution of pseudocapacitive behaviour at different scanning rates. When the scanning rates were 0.1mV·s^{-1}, 0.3mV·s^{-1}, 0.5mV·s^{-1}, 0.8mV·s^{-1} and 1.0mV·s^{-1}, the pseudocapacitive contributions were 49.2%, 59.8%, 67.9%, 72.8% and 80.6%, respectively. These results indicated that the capacity of Fe_2O_3@3DGF was mainly controlled by the pseudocapacitive behaviours which suggested a high kinetic process and rate capacity [5]. The high conductivity and contact area of Fe_2O_3 provided abundant effective sites that facilitated electrolyte adsorption. These contributed to the improvement in the capacitive-controlled behaviour of the prepared material [6]. Figure 6d showed a detailed pseudocapacitive contribution proportion value in CV curve at the scanning rate of 0.5mV·s^{-1}(dark color identification in the figure).

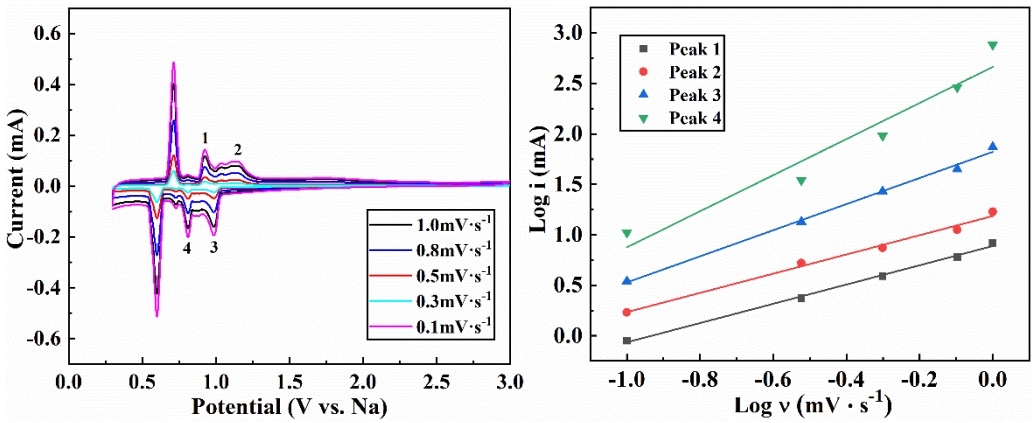

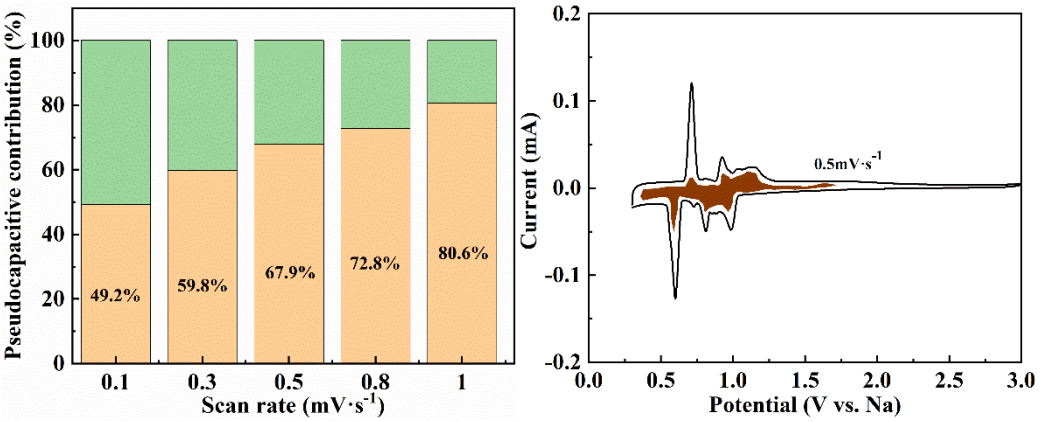

Figure 6. Kinetics investigation of the as-prepared Fe_2O_3@3DGF (a) CV curves at different scan rates (b) corresponding $log\ i$ vs. $log\ v$ plots at each redox peak (c) bar chart exhibiting the contribution ratio of pseudocapacitive contribution (d) CV curve with the pseudocapacitive contribution shown at a scan rate of 0.5mV·s^{-1}

To further investigate the observed differences in cycling stability and rate performance of Fe_2O_3@3DGF, the morphology and structure of the electrode material after 200 cycles were characterized by SEM. The results were shown in Figure 7. The surface of the Fe_2O_3@3DGF electrode material was very flat after 200 cycles of charging and discharging with no obvious cracks (Figure 7a). These characteristics were beneficial for maintaining good electrochemical and cycling stabilities. Although the rod-shaped Fe_2O_3@3DGF was fused with the base material 3DGF, the initial rod-shaped morphology was maintained. The flat top feature was still observed which indicated that this composite structure was stable. The stable structure retained the original morphology. Therefore, it was believed that this structural feature was related to the Fe-O-C bond formed between graphene surface and Fe_2O_3. Hence, the Fe_2O_3@3DGF both maintained a stable connection between Fe_2O_3 nanorods and 3DGF sheets and promoted the electrochemical reaction kinetics of the electrodes. These significantly enhanced the sodium-ion battery performance of Fe_2O_3@3DGF complexes.

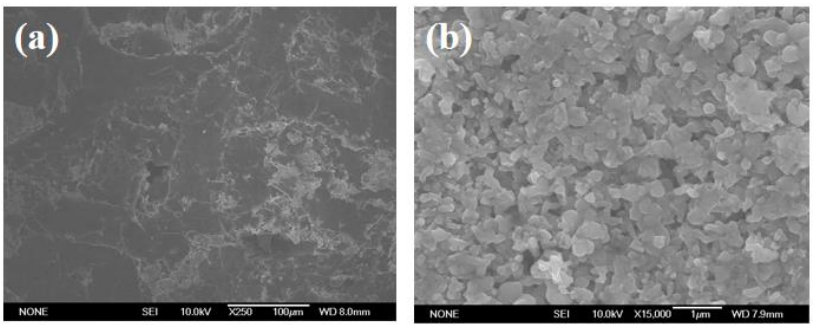

(a) Low-magnification (b) High-magnification

Figure 7. SEM images of Fe_2O_3@3DGF after charging-discharging 200 cycles

The electrochemical properties of the prepared Fe_2O_3@3DGF were compared with samples described in literature. The findings were summarized in Table 1. Fe_2O_3@3DGF with a unique nanorod structure was tightly connected with the 3D graphene foam skeleton. It had better cycle stability and specific capacity than the samples described in the literature. Therefore, it was clear that the three-dimensional graphene foam skeleton as the matrix material of Fe_2O_3@3DGF nanorods improved electrochemical performance.

Table 1. The electrochemical performance of Fe_2O_3@3DGF in this work compared with the reported Fe_2O_3 based composites

Matetial	Current Density ($mA \cdot g^{-1}$)	Cycles	Retention Capacity ($mA \cdot g^{-1}$)	Ref.
Fe_2O_3@C	200	100	210	[19]
γ- Fe_2O_3 thin film	475	80	335.2	[22]
Fe_2O_3-S@C	800	100	224	[30]
Fe_2O_3@3DGF	500	200	398	this paper

4. CONCLUSIONS

The precursor α-FeOOH@3DGF was annealed at different temperatures. The resulting Fe_2O_3@3DGF showed good cycle stability and high-rate performance. The capacity of Fe_2O_3@3DGF was mainly controlled by the pseudocapacitive behaviours which indicated high kinetic process and rate capacity. The surface of the Fe_2O_3@3DGF electrode material was very flat even after 200 cycles of charging and discharging with no obvious cracks. These characteristics were beneficial for maintaining good electrochemical and cycling stabilities.

References

1. W.J. Zhu, Y.Y. Wang, Y.Z. Yu, Y.H. Hu and Y.C. Chen, *J. Alloy. Compd.,* 813 (2020) 152175.
2. C. Zhang, L. Shen, J.Q. Shen, F. Liu. G.Chen, R. Tao, S.X. Ma, Y.T. Peng and Y.F. Lu, *Adv. Mater.*, 31 (2019) 1808338.
3. B.Huang, Z.F. Pan, X.Y. Su and L. An, *J. Power Sources,* 399 (2018) 274.
4. F. Gu, J.F. Guo, X. Yao, P.A. Summers, S.D. Widi and P. Hall, *J. Clean. Prod.,* 161 (2017) 765.
5. L.Y. Wang, L.Q. Liu, C.C. Zhang, X. Wang and X.Y. Li, *Int. J. Electrochem. Sci.,* 16 (2021) 210643.
6. L.Y. Wang, C.C. Zhang, L.Q. Liu and X. Wang, *J. Mater. Sci.: Mater. Electron.*, 32 (2021) 15665.
7. J. Zhou, J.C. Chen, M.X. Chen, J. Wang, X.Z. Liu, B. Wei, Z.C. Wang, J.J. Li, L. Gu, Q.H. Zhang, H. Wang and L. Guo, *Adv. Mater.*, 1 (2019) 1807874.
8. L.Y. Wang, B.W. Wang, Y.C. Yang, X. Chen, J.H. Hu, D. Yang and A.G. Dong, *Chem. Commun.*, 55 (2019) 1229.

9. L.Y. Wang, Y.L. Zhang, D.P. Li, X. Wang and X.Y. Li, *Int. J. Electrochem. Sci.*, 16 (2021) 211059.
10. F. Kong, L. Lv, Y. Gu, S. Tao, X. Jiang, B. Qian and L. Gao, *J. Mater. Sci.*, 54 (2019) 4225.
11. Z. Zhang, X. Shi, X. Yang, Y. Fu, K. Zhang, Y. Lai and J. Li, *ACS Appl. Mater. Interface*s, 8 (2016) 13849.
12. X. Ou, C. Yang, X. Xiong, F. Zheng, Q. Pan, C. Jin, M. Liu and K. Huang, *Adv. Funct. Mater.*, 27 (2017)1606242.
13. K. Zhang, M. Park, L. Zhou, G.H. Lee, J. Shin, Z. Hu, S.L. Chou, J. Chen and Y.M. Kang, *Angew. Chem.Int. Edit.*, 55 (2016) 12822.
14. R. Alcantara, M. Jaraba, P. Lavela and J.L. Tirado, *Chem. Mater.*, 14 (2002) 2847.
15. Q. Li, X.T. Guo, M.B. Zheng and H. Pang, *Funct. Mater. Lett.*, 11 (2018) 1840004.
16. S. Boyd and V. Augustyn. *Inorg. Chem. Front.*, 5 (2018) 999.
17. J. Mosa, F.J. Garcia-Garcia, A.R. Gonzalez-Elipe and M. Aparicio, *Nanomaterials*, 11 (2021) 966.
18. S.G. Dai, Y.C. Bai, W.X. Shen, S. Zhang, H. Hu, J.W. Fu, X.C. Wang, C.G. Hu and M.L. Liu, *J. Power Sources.*, 482 (2021) 228915.
19. B.B. Wang, S.P. Zhang, G. Wang, H. Wang and J.T. Bai, *J. Colloid Interface Sci.*, 557 (2019) 216.
20. Y. Su, B. Fu, G.L. Yuan, M. Ma and J.Y. Li, *Nanotechnology*, 31 (2020) 155401.
21. Z.L. Jian, B. Zhao, P. Liu, F.J. Li, M.B. Zheng, M.W. Chen, Y. Shi and H.S. Zhou, *Chem. Commun.*, 50 (2014) 1215.
22. D. Nayak, S. Puravankar, S. Ghosh and V. Adyam, *Ionics*, 25 (2019) 5857.
23. L. Yin, Y.Z. Pan, M.Q. Li, Y.X. Zhao and S.H. Luo, *Nanotechnology*, 31 (2020) 155402.
24. K.Q. Zhou, Y.C. Zhen, Z.S. Hong, J.H. Guo and Z.G. Huang, *Mater. Lett.*, 190 (2017) 52.
25. Y.J. Chen, X.T. Yuan, C. Yang, Y.B. Lian, A.A. Razzaq, R. Shah, J. Guo, X.H. Zhao, Y. Peng and Z. Deng, *J. Alloy. Compd.*, 777 (2019) 127.
26. M. Ma, L.Y. Cao, H. Qi, K. Yao, J.F. Huang, Z.W. Xu, S.Y. Chen and J.Y. Li, *J. Alloy. Compd.*, 808 (2019)151657.
27. F. Wang, C.Q. Wang, H. Chen, W.L. Zhang, R.J. Jiang, Z.H. Yan, Z.Y. Huang, H.H. Zhou and Y.F. Kuang, *Nanotechnol.*, 30 (2019) 335701.
28. M. Huang, C. Chen, S. Wu and X. Tian, *J. Mater. Chem. A*, 5 (2017) 23035.
29. P. Xiao, F. Bu, R. Zhao, M. F. Aly, I. Shakir and Y. Xu, *ACS Nano*, 12 (2018) 3947.
30. J. Li, S.L. Wang, X.L. Chen, T. Xiao, X.Y. Tan, P. Xiang and L.H. Jiang, *Electrochim. Acta*, 290 (2018) 332.